

A Top-down Strategy to Engineer Active Layer Morphology for Highly Efficient and Stable All-polymer Solar Cells

Huiting Fu, Zhengxing Peng, Qunping Fan, Francis R. Lin, Feng Qi, Yixin Ran, Ziang Wu, Baobing Fan, Kui Jiang, Han Young Woo, Guanghao Lu, Harald Ade,* and Alex K.-Y. Jen*

Dr. H. Fu, K. Jiang, Prof. A. K.-Y. Jen,

Department of Materials Science and Engineering, City University of Hong Kong, Kowloon 999077, Hong Kong

*E-mail: alexjen@cityu.edu.hk

Dr. Z. Peng, Prof. H. Ade

Department of Physics and Organic and Carbon Electronics Laboratories (ORaCEL), North Carolina State University, Raleigh, NC 27695, USA

*E-mail: hwade@ncsu.edu

Dr. Q. Fan, Dr. F. R. Lin, F. Qi, Dr. B. Fan, Prof. A. K.-Y. Jen

Department of Chemistry, City University of Hong Kong, Kowloon 999077, Hong Kong

Y. Ran, Prof. G. Lu

Frontier Institute of Science and Technology, Xi'an Jiaotong University, Xi'an 710054, P. R. China

This is the author manuscript accepted for publication and has undergone full peer review but has not been through the copyediting, typesetting, pagination and proofreading process, which may lead to differences between this version and the [Version of Record](#). Please cite this article as doi: [10.1002/adma.202202608](https://doi.org/10.1002/adma.202202608).

This article is protected by copyright. All rights reserved.

Z. Wu, Prof. H. Y. Woo

Department of Chemistry, College of Science, Korea University, Seoul 136-713, Republic of Korea

Dr. H. Fu, Dr. Q. Fan, Dr. F. R. Lin, F. Qi, Dr. B. Fan, K. Jiang, Prof. A. K.-Y. Jen

Hong Kong Institute for Clean Energy, City University of Hong Kong, Kowloon 999077, Hong Kong

Prof. A. K.-Y. Jen

Department of Materials Science and Engineering, University of Washington, Seattle, Washington 98195-2120, United States

Keywords: All-polymer solar cells, layer-by-layer deposition, blend morphology, power conversion efficiencies, stability

Abstract

A major challenge hindering the further development of all-polymer solar cells (all-PSCs) employing polymerized small-molecule acceptors is the relatively low fill factor (FF) due to the difficulty in controlling active layer morphology. The issues typically arise from oversized phase separation resulting from the thermodynamically unfavorable mixing between two macromolecular species, and disordered molecular orientation/packing of highly anisotropic polymer chains. Herein, a facile top-down controlling strategy to engineer the morphology of all-polymer blends is developed by leveraging the layer-by-layer (LBL) deposition. Optimal intermixing of polymer components could be achieved in the two-step process by tuning the bottom-layer polymer swelling during top-layer

This article is protected by copyright. All rights reserved.

deposition. As a result, both the molecular orientation/packing of bottom layer and the crystallinity of top layer can be optimized with a suitable processing solvent for the top layer. Consequently, a favorable morphology with gradient vertical composition distribution for efficient charge transport and extraction is realized, affording a high all-PSC efficiency of 17.0% with a remarkable FF of 76.1%. The derived devices also possess excellent long-term thermal stability which can retain >90% of their initial efficiencies after being annealed at 65 °C for 1300 h. These results validate that the distinct advantages of employing such LBL processing protocol to fabricate high-performance all-PSCs.

1. Introduction

All-polymer solar cells (all-PSCs) comprising semiconducting polymers as both donor and acceptor have attracted tremendous interest due to their superior morphological stability and mechanical conformability over the organic photovoltaics that are based on small-molecule acceptors (SMAs).^[1-3] Recent reports have shown some emerging applications of all-PSCs in flexible and wearable electronics.^[4,5] However, all-PSCs were confronted by inferior power conversion efficiencies (PCEs) in earlier developments primarily due to the lack of high-performing *n*-type polymers and the hard to control active layer morphology.^[6] Encouragingly, the recent vigorous development of polymerized SMAs (PSMAs) has led to significant breakthroughs in the all-PSCs field to enable PCEs to go beyond 16%.^[7-15] Although the rationally designed polymer acceptors have gradually improved the performance of all-PSCs, they are still hampered by the relatively low fill factor (FF) and short-circuit current density (J_{sc}) compared to those of better performing SMA-based devices.^[16-19] Considering that morphology control exerts a significant effect on enhancing the device parameters of J_{sc} and particularly FF, it is critical to develop strategies to manipulate the microstructural features in all-polymer blends to further improve all-PSC efficiencies.

This article is protected by copyright. All rights reserved.

Conventionally, constructing a nanoscale phase-separated bulk-heterojunction (BHJ) morphology in active layers to reach balanced exciton dissociation and charge transport is a prerequisite to ensure efficient cell performance.^[20-22] Such an architecture is generally realized by casting a pre-mixed solution, which involves a quite complicated three-phase interplay during film deposition dictated by different crystallization and thermodynamic properties of materials. This issue becomes notoriously severe in all-PSCs containing two macromolecular species, where the absence of entropic driving force for intermixing and the complex interactions between polymer species make it highly challenging to control the phase separation.^[7] Another critical issue for all-PSCs refers to the non-optimal molecular packing and interfacial orientation in the composite composed of long but highly anisotropic conjugated polymer chains, which strongly affects the charge generation and collection in devices.^[23-26] Therefore, it is essential to develop a strategy to precisely regulate the phase separation and polymer packing/orientation to realize high-efficiency all-PSCs.

The two-step layer-by-layer (LBL) processing approach has been identified earlier to circumvent the complicated morphology evolution associated with conventional one-step deposition.^[27-31] During the deposition of top layer on bottom layer, the swelling of bottom layer induces the interdiffusion between different components and enables the formation of functional heterojunction framework. This provides an opportunity to overcome the limitations arising from intrinsic thermodynamic properties of materials, especially for all-polymer systems with insufficient miscibility between different species.^[32-34] Moreover, such a two-step procedure allows the donor and acceptor to be deposited independently, which can broaden the processing window for fine-tuning polymer packing.^[35-41]

However, so far only few successful cases have been shown in fabricating high-performance all-

This article is protected by copyright. All rights reserved.

PSCs with LBL technique, mainly due to the following two factors: 1) most of high-performing polymers possess similar solubilizing properties, therefore the bottom layer could just be dissolved and washed out during deposition of top layer instead of being controllably swollen; 2) the long-range order and aggregation of the bottom layer could be affected during casting of top layer, resulting in inadequate molecular packing order and consequently a low-quality LBL film. To overcome these limitations, we need to develop new controlling techniques in conjunction with new polymers for LBL processing in order to optimize the all-polymer blend morphology for achieving high efficiencies.

Herein we present a top-down strategy to engineer all-polymer active layer morphology utilizing a LBL processing technique, where highly crystalline polymer donor D18 and a modified Y6-derived PSMA named PY-FT are introduced as the bottom layer and top layer, respectively. By combining different processing solvents for bottom and top layers, it realizes controlled swelling of the D18 bottom layer, facilitating desirable intermixing with PY-FT top layer to alleviate the severe phase separation observed in conventional BHJ films. Therefore, a well-defined vertical phase distribution is formed, benefitting the charge carriers generation and transport. More importantly, an appropriate top-layer solvent not only contributes to improved crystallinity of the PY-FT top layer, but also ameliorates the molecular orientation/packing of the D18 bottom layer. Benefiting from these advantages, the resulting all-PSCs achieved a PCE of 17.0% with an outstanding FF of 76.1%, representing one of the highest efficiencies reported so far for binary all-PSCs. All-PSCs based on the top-down strategy exhibit an excellent thermal stability retaining over 90% of initial performance after annealing at 65 °C for 1300 h. Our work renders the control of all-polymer blend morphology a more tractable problem, and paves a new avenue to the fabrication of high-performance all-PSCs.

This article is protected by copyright. All rights reserved.

2. Results and Discussion

2.1. Polymer Properties and Photovoltaic Device Performance

The chemical structures of D18 and PY-FT are shown in **Figure 1a**. The polymer acceptor PY-FT was designed by replacing the *n*-undecyl in PY2S-F^[13] with a shorter *n*-nonyl to enhance structural order in the corresponding SMA derivatives.^[42] The detailed characterizations are provided in the Supporting Information. The polymer donor D18 was synthesized according to reference^[43] with a number-average molecular weight of 65.0 kDa (PDI = 2.17). Such D18 exhibits sufficient solubility in heated chlorobenzene (CB, 7 mg/mL, 80 °C) and chloroform (CF, 5mg/mL, 40 °C) to give a viscous solution, but is almost insoluble in toluene (TL) even at elevated temperature. Meanwhile the polymer acceptor PY-FT is well soluble (15 mg/mL) in all above mentioned solvents at room temperature. The optical absorption of PY-FT film complements very well to that of D18 film, and the frontier molecular orbital energy levels between them are also well-matched (**Figure S2**), which can facilitate the efficient generation of charge carriers. Variable-temperature UV-vis absorption spectra of D18 and PY-FT in dilute solutions were also measured to probe their temperature-dependent aggregation properties. As shown in **Figure 1b**, both polymers display strong tendency to self-aggregate, which might cause difficulties in achieving adequate intermixing during spin-coating of their pre-mixed solution.

To evaluate the photovoltaic performance of D18:PY-FT blend, conventional all-PSCs were first fabricated with an architecture of indium tin oxide (ITO)/poly(3,4-ethylenedioxythiophene):poly(styrene sulfonate) (PEDOT:PSS)/active layer/poly[(9,9-bis(3'-(N,N-dimethylamino)propyl)-2,7-fluorene)-*alt*-5,5'-bis(2,2'-thiophene)-2,6-naphthalene-1,4,5,8-

tetracaboxylic-*N,N'*-di(2-ethylhexyl)imide] (PNDIT-F3N)/silver (Ag), employing common processing solvents of CB and CF. **Figure 1d** shows the representative current density versus voltage (*J*-*V*) curves and **Table 1** summarizes the related photovoltaic parameters of derived BHJ devices. All-PSCs prepared from CB yield a moderate PCE of 13.9% with a high open-circuit voltage (*V*_{oc}) of 0.940 V, a *J*_{sc} of 21.6 mA cm⁻², and a FF of 68.5%. Dramatic changes in solar cell performance are observed when the processing solvent is shifted from CB to CF. The resulting devices show simultaneously increased *J*_{sc} (23.1 mA cm⁻²) and FF (72.3%), enhancing the PCE to 15.4% despite of a slightly decreased *V*_{oc} (0.923 V). These results reveal that the performance of D18:PY-FT system is greatly hinged on the film fabrication conditions.

Further attempts were made from processing perspectives to optimize the active layer morphology to improve device efficiency. The LBL approach was employed due to its distinct advantages in the processing of highly crystalline materials.^[29] As illustrated in **Figure 1c**, D18 dissolved in CB was first deposited on ITO/PEDOT:PSS substrate and left unperturbed for solvent evaporation, followed by casting the PY-FT solution on top. It should be noted that the morphology of such LBL film is largely determined by the properties of top-layer processing solvent, which significantly influence the crystalline feature of top-layer material and the degree of interdiffusion between bottom and top layers.^[44,45] By taking these factors into consideration, we carefully selected CF and TL solvents to establish the comparison on preparing the PY-FT top layer. These two solvents have notably different boiling points, volatility and solubilizing strength to the D18 bottom layer (**Figure S3**), therefore can lead to different interdiffused microstructures in the corresponding LBL films. Note that from appearance the D18 film was not eroded by spin-coating CF or TL on top (**Figure S4**). As a result, both two types of LBL devices outperform their BHJ counterparts. LBL devices

with top layer processed by CF deliver an outstanding PCE of 16.2%, benefitted from the clearly enhanced J_{sc} (23.6 mA cm^{-2}) and FF (73.5%). Moreover, the LBL deposition using TL as the top-layer processing solvent, which vaporizes much slower and has lower solubility for D18 than CF, enables the devices to have elevated J_{sc} and FF values to 24.2 mA cm^{-2} and 76.1%, respectively to afford a very high PCE of 17.0%. To the best of our knowledge, the PCE and FF are among the highest values reported for binary all-PSCs to date (**Figure S5**). These promising results validate that LBL processing is an effective strategy for optimizing morphology to enhance device performance. The general applicability of this approach has also been evaluated on several other material systems which show similar improvements (**Figure S6**, **Figure S7**, and **Table S1**). In the following discussion, four types of all-PSCs fabricated under different conditions are denoted as BHJ-CB, BHJ-CF, LBL-CF, and LBL-TL, respectively, to simplify the description.

As shown in **Figure 1e**, external quantum efficiency (EQE) spectra of the optimal BHJ-CB, BHJ-CF, LBL-CF, and LBL-TL devices were recorded, all of which covered a broad range from wavelength of 300 to 900 nm. Moreover, the EQE values increase subsequently across almost the whole window of spectral response, from BHJ-CB, BHJ-CF, LBL-CF to LBL-TL. This suggests that both donor D18 and acceptor PY-FT show more efficient incident photon-to-current conversion depending on the morphological evolution. Consequently, the LBL-TL devices yield the highest integrated J_{sc} (23.6 mA cm^{-2}) compared to those of BHJ-CB (20.9 mA cm^{-2}), BHJ-CF (22.3 mA cm^{-2}), and LBL-CF (22.9 mA cm^{-2}) devices. The gradual increasing of integrated J_{sc} values in the order of BHJ-CB, BHJ-CF, LBL-CF, and LBL-TL is consistent with those obtained from the J - V measurements.

2.2. Investigation of the Dynamics of Charge Generation, Transport, and Recombination

This article is protected by copyright. All rights reserved.

The varied J_{sc} and FF values are the main factors accounting for the different PCEs attained in four types of all-PSCs. To understand the causes of the differences, the electron (μ_e) and hole (μ_h) mobilities in four blends were measured by the space-charge-limited-current (SCLC) method. As shown in **Figure S8** and **Table S2**, the average μ_h of the four blends are in the similar range of $7.85 \times 10^{-4} - 8.81 \times 10^{-4} \text{ cm}^2 \text{V}^{-1} \text{s}^{-1}$. However, an increasing trend in their average μ_e values is shown as BHJ-CB ($2.86 \times 10^{-4} \text{ cm}^2 \text{V}^{-1} \text{s}^{-1}$) < BHJ-CF ($3.77 \times 10^{-4} \text{ cm}^2 \text{V}^{-1} \text{s}^{-1}$) < LBL-CF ($4.48 \times 10^{-4} \text{ cm}^2 \text{V}^{-1} \text{s}^{-1}$) < LBL-TL ($6.26 \times 10^{-4} \text{ cm}^2 \text{V}^{-1} \text{s}^{-1}$). Photo-induced charge extraction by linearly increasing voltage (photo-CELIV) was applied to further estimate the carrier mobility (μ) in optimum BHJ and LBL devices (**Figure S11**, **Table S5**). The μ of the LBL-TL device is $5.79 \times 10^{-4} \text{ cm}^2 \text{V}^{-1} \text{s}^{-1}$, which is larger than that of $3.68 \times 10^{-4} \text{ cm}^2 \text{V}^{-1} \text{s}^{-1}$ from BHJ-CF device. The higher carrier mobility and more-balanced charge transport (**Figure 1f**) should contribute to the higher J_{sc} and FF values obtained from LBL cells relative to those of BHJ ones.

To gain deeper insight into the improved performance of devices prepared from LBL approach, we further assessed the charge generation and recombination mechanism in these all-PSC devices. The photocurrent density (J_{ph}) versus the effective voltage (V_{eff}) curves were probed to determine the charge dissociation probability ($P(E,T)$) (**Figure S12** and **Table S6**). For all devices, the J_{ph} reaches saturation (J_{sat}) at a high V_{eff} of 2 V, which means all the generated excitons are split and the resultant free charge carriers are collected subsequently. Under the maximal power output and short-circuit conditions, LBL-CF and LBL-TL devices exhibit higher $P(E,T)$ values of 84.3%/95.6% and 84.6%/96.4%, respectively, than BHJ-CB (75.9%/93.2%) and BHJ-CF (81.8%/95.1%) devices. Meanwhile, transient photocurrent (TPC) measurement (**Figure S14a**) shows that LBL-CF and LBL-TL devices yield a shorter charge extraction time than those of BHJ-CB and BHJ-CF ones, suggesting a faster charge extraction

rate. These combined results validate the more efficient exciton dissociation and charge extraction in LBL devices. Transient photovoltage (TPV) measurement was further conducted to analyze the charge recombination dynamic by recording the voltage decay under open-circuit condition. As depicted in **Figure S14b**, the extracted carrier lifetimes are 46.9, 55.0, 64.7, and 69.1 μ s for cells based on BHJ-CB, BHJ-CF, LBL-CF, and LBL-TL, respectively. The prolonged decay lifetime of carriers in LBL devices indicates that the charge recombination is mitigated to a certain extent compared to that of BHJ cases, supporting their higher EQE and FF values.

2.3. Investigation of Phase Separation

Achieving proper phase separation between two constituent polymers, including phase distribution, and domain size and purity, is crucial for establishing favorable morphology to realize high-performance all-PSCs. To study the correlations between processing methods and morphology of blends, film-depth-dependent light absorption spectrometry (FLAS), transmission electron microscopy (TEM) and resonant soft X-ray scattering (RSoXS) were performed to systematically unravel the influence of different processing protocols on the microstructural features in BHJ-CB, BHJ-CF, LBL-CF, and LBL-TL films.

First, the vertical distributions of D18 and PY-FT in four types of blend films were quantitatively investigated by FLAS, which is a well-established technique for mapping composition profile, morphology, and optical/electronic properties along film-depth direction.^[46,47] As can be found in the FLAS results shown in **Figure 2a**, in all samples, the position of D18 absorption peaks remains almost consistent throughout the whole film, indicating the similar crystallinity of D18 at different depths, which may help reduce energetic disorder and maintain the integrity of hole-transport channels in

the blend.^[46] On the other hand, the absorption profiles of PY-FT show apparent variations at different depths, indicating disorders may arise and undermine the vertical electron transport in the blend. Notably, the shifting of PY-FT absorption peaks with variable film depths shows different trends between BHJ and LBL films, which is likely due to their distinct PY-FT distribution.

Upon fitting the FLAS plots with the absorption spectra of neat D18 and PY-FT films, the composition ratio of D18 and PY-FT at different film-depths can be extracted, as depicted in **Figure 2b**. While the two BHJ films show rather uniform phase distribution throughout the entire active layer vertically, the two LBL films feature distinctly different vertical phase segregation, wherein D18 and PY-FT both display a gradient distribution with higher concentrations of D18 near the anode and PY-FT near the cathode, respectively. Furthermore, contact angle measurements also show that PY-FT is more enriched at the cathode interface in LBL films compared to BHJ films (**Figure S16, Table S7**). These results show that LBL processing is capable of creating a favorable vertically gradient phase distribution that is similar to p-i-n structure to facilitate charge extraction and field-assisted charge transport in the devices.

It is notable that the LBL-TL film exhibits more pronounced vertical gradient distribution of polymer species compared to LBL-CF, with 88.1 wt% PY-FT content on the top surface and 79.6 wt% D18 content at the bottom surface. This can be attributed to the fact that the formation of functional heterojunction in LBL process is largely relied on swelling of the bottom layer induced by the top-layer processing solvent, facilitating quasi-solid-state interdiffusion of two materials.^[48] When a more solubilizing solvent for D18 such as CF is used for depositing PY-FT top layer, it swells D18 significantly to allow large amounts of PY-FT to be diffused into the D18 bottom layer. While TL is used as the processing solvent for PY-FT, the reduced degree of swelling inhibits the diffusion of PY-FT to

penetrate all the way into the D18 domain due to limited solubility of TL to D18, leading to lesser degree of PY-FT penetrating downward compared to that in LBL-CF. In this regard, the controllable swelling of bottom-layer polymer by choosing an appropriate top-layer depositing solvent in LBL processing provides an extra mechanism to engineer blend morphology.

Additionally, the exciton generation contour within the actual photovoltaic cells derived from four types of blends was numerically simulated by combining the information from FLAS with an optical transfer matrix model reported previously.^[46] As shown in **Figure 2c**, higher number of excitons are generated in D18 phase (~550 nm) near the anode region in the LBL devices compared to the BHJ ones, corresponding to the locally enriched donor. Nevertheless, most of the photons harvested by PY-FT phase (700-900 nm) are converted to excitons in the bottom-half active layer for all four types of devices. The exciton generation rate profiles (**Figure S17**) also prove that excitons are mainly generated at the bottom-half part of active layers. Such scenario suggests that the electrons generated from exciton dissociation may need to travel across tens-of-nanometer distance before reaching the cathode. Under such circumstances, the distribution of acceptor-rich phase in the top-half region of active layer in the LBL devices facilitates the electron transport and collection. The results resonant well with the previously discussed charge extraction and recombination dynamics achieved for the LBL processed devices.

The results obtained from TEM further help visualize the bulk phase framework within BHJ-CB, BHJ-CF, LBL-CF, and LBL-TL blends (**Figure 3a**). It can be seen that all four types of blends show different phase-separated morphologies. In the BHJ-CB film, excessive aggregations of D18 and PY-FT induce over-sized (40-70 nm) phase separation that is unfavorable for exciton diffusion/dissociation and thereby leads to the lowest $P(E,T)$ among four cases. In the BHJ-CF film, the degree of polymer

aggregation was reduced due to much faster evaporation of CF than CB, leading to a smaller scale phase separation. On the contrary, well-defined phase separation and bicontinuous networks are formed in the LBL films due to the percolation behavior during LBL processing, helping the resulting devices to achieve excellent performance. Moreover, the distinct phase separation between LBL-CF and LBL-TL films further validates the impact of top-layer depositing solvents on the resulting active layer morphology.

RSoXS was then conducted utilizing X-ray with a photon energy of 284 eV to estimate the relative purity and average size of domains in four types of blends, as shown in **Figure 3b** and **Table 2**. The relative integrated scattering intensity (ISI) is proportional to the root-mean-square composition variations, which are monotonically related to the average phase purity. Among all cases, BHJ-CB has the highest ISI, therefore the ISIs of other blends are normalized to that of BHJ-CB for relative comparison. As a result, the domain purity for four types of blends exhibits in a sequence of BHJ-CB > BHJ-CF > LBL-CF > LBL-TL, which is in the opposite trend with their corresponding FF values (**Figure 3c**). The reason stems from the inadequate miscibility in these all-polymer systems being lower than the electron percolation threshold,^[49,50] as the poor polymer-polymer miscibility typically leads to excessive phase separation with reduced percolation. Therefore, a lower domain purity which resembles better intermixing of polymers is preferred to be closer to the electron percolation threshold. This may lead to higher FF in the cases with lower domain purity, as shown in an increasing trend of FF values for BHJ-CB < BHJ-CF < LBL-CF < LBL-TL devices.

On the other hand, all four types of blends exhibit two predominant scattering peaks (labeled as peak 1 and peak 2) in their RSoXS profiles, and the corresponding long period of phase separation related to the center-to-center domain spacing can be estimated from peak locations. The calculated

long period values of peak 1 for BHJ-CB, BHJ-CF, LBL-CF, and LBL-TL are 95, 90, 169, and 131 nm, respectively, which correspond to domain sizes of 47.5, 45.0, 84.5, and 65.5 nm, respectively. These numbers are apparently exceeding the typical exciton diffusion length of 10-20 nm in most of organic conjugated materials.^[51,52] It is also notable that LBL films possess larger domain sizes compared to BHJ ones, echoing with the local enrichment of PY-FT and D18 in LBL films observed by FLAS studies. However, the long period values of peak 2 are similar in all four types of blends, showing a much smaller domain size of ~14 nm within reasonable exciton diffusion lengths. It is reported that larger volume fraction of such size of domains is advantageous for obtaining higher device performance.^[53] Here, the volume fractions of these smaller domains are in an increasing order of BHJ-CB < BHJ-CF < LBL-CF < LBL-TL (**Figure 3d**), which agrees well with the gradually improved J_{sc} values in the corresponding all-PSCs.

Based on the FLAS, TEM and RSoXS analysis, it can be concluded that the deposition of donor and acceptor polymers in a sequential manner generates a preferred vertical phase distribution with enriched polymer donor fraction near the anode and enriched polymer acceptor fraction near the cathode. The tunable swelling of the bottom layer enabled by a suitable top-layer depositing solvent facilitates better intermixing between polymer species, helping alleviate the oversized domains in BHJ films to afford a more favorable morphology for facilitating charge carriers generation, transport and collection.

2.4. Analysis of Molecular Packing and Orientation

Knowing that the top-layer processing solvent profoundly affects the swelling of D18, we further studied the molecular packing of D18 to see if it was changed during the casting of top layer. Grazing-

incidence wide-angle X-ray scattering (GIWAXS) measurements were performed to provide information about the molecular packing and orientation in as-cast D18 film and D18 films post-treated with neat solvents of CF or TL to mimic device fabrication conditions. **Figure 4a** shows the two-dimensional (2D) GIWAXS patterns of the three D18 films, and the corresponding line-cut profiles in the out-of-plane (OOP) and in-plane (IP) directions are depicted in **Figure S18**. The relevant crystallographic parameters are listed in **Table S8**. The as-cast D18 presents an intense (010) peak from π - π stacking along the OOP direction at 1.77 \AA^{-1} and a sharp lamellar (100) peak along the IP direction at 0.345 \AA^{-1} , indicative of its preferential face-on orientation with respect to the substrate. Furthermore, higher-order (002) and (004) diffraction peaks respectively located at $q_{xy}=0.57$ and 1.13 \AA^{-1} can be easily identified in D18 packing motifs. These unique (00l) reflections imply strong extension of D18 main chain and extremely excellent crystalline ordering along the backbone.

Intriguingly, a clear lamellar (200) scattering signal at $q_z=0.701 \text{ \AA}^{-1}$ only appear in the TL-treated D18, reflecting its improved molecular ordering or more face-on molecular orientation compared to the as-cast and CF-treated ones. To further explore the effects of solvent treatment on the orientation of D18 molecular packing, the pole figures extracted from (100) and (010) scattering signals of the three D18 films were plotted, from which the ratio of face-on and edge-on orientation can be quantified (**Figure 4b** and **Figure S19**). Both datasets reveal that D18 possesses a substantially increased face-on/edge-on proportion after being treated by CF or TL, while TL-treated D18 is found to present a greater extent of face-on geometries than the CF-treated one, meaning that TL treatment is more effective in terms of tweaking the polymer orientation to facilitate vertical transport of free charge carriers to the electrodes. All these changes may stem from the

rearrangement of D18 in amorphous regions of lower density during swelling.^[34,48] The results from atomic force microscopy (AFM) study also revealed the impact of different top-layer processing solvents on the microstructure of bottom-layer D18 films (see **Figure S20**). In addition, the change in packing pattern of D18 before and after solvent treatment was further corroborated by UV-vis absorption measurements (**Figure S21**). The TL-treated D18 exhibits almost unchanged absorption intensity of 0-1 transition over that of 0-0 transition (I_{0-1}/I_{0-0}) relative to the as-cast D18 film. In stark contrast, the I_{0-1}/I_{0-0} increases obviously upon CF treatment, indicating the reduced aggregation strength in CF-treated D18 film. SCLC measurements of the three D18 films also support the aforementioned results (**Figure 4c**). These phenomena show that a suitable top-layer processing solvent for LBL processing is also capable of ameliorating the crystallinity and molecular orientation of bottom-layer materials.

Following the D18 bottom layer, we also investigated the morphology and crystallization behaviors of PY-FY processed from CF and TL in addition to the four types of BHJ and LBL blends by GIWAXS to understand where their different performance stem from. The 2D and line-cut GIWAXS profiles are provided in **Figure S22** and **Figure 4d**, respectively. The two PY-FT films exhibit preferred face-on orientation in their backbone stacking as supported by the intensive (010) scattering peak at around 1.59 \AA^{-1} in the OOP direction, corresponding to a π -distance of 3.95 \AA . However, the TL-processed PY-FT film attains a larger coherence length (CCL) (14.6 \AA) than that processed from CF (13.2 \AA), since the higher boiling point of TL may further prolong drying time to allow PY-FT to pack better in the film, as evidenced by the enhanced μ_e from 6.81×10^{-4} to $8.95 \times 10^{-4} \text{ cm}^2 \text{ V}^{-1} \text{ s}^{-1}$ (**Figure S10** and **Table S4**). Notably, previous reports reveal that aligning the conjugated donors and acceptors at the interfaces affects the free charge carrier generation in all-PSCs due to the planar

structures of polymers.^[3,54] Thus, the relatively higher fraction of face-on crystallites in TL-treated D18 would promote favorable contacts with the face-on dominated PY-FT crystallites at their interfaces to facilitate exciton separation, as evidenced by the increased $P(E,T)$ and J_{sc} in LBL-TL devices.

In all the blend films, both D18 and PY-FT preserve their packing patterns as in neat films, maintaining their own crystalline properties even after mixing. The CCL values of the overall $\pi\text{-}\pi$ stacking along the OOP direction were calculated to be 29.0, 26.5, 26.8 and 27.3 Å for BHJ-CB, BHJ-CF, LBL-CF, and LBL-TL, respectively. The largest CCL obtained in BHJ-CB corresponds to the most large-scale phase separation and highest domain purity. The clearly decreased CCL in BHJ-CF over that of BHJ-CB indicates formation of smaller-sized phase separation at the expense of reduced crystallinity. However, LBL films display intensive diffraction intensity together with a larger CCL, and thus higher crystallinity compared to the higher-performance BHJ film (BHJ-CF), implying that the LBL processing may not only control the extent of the phase separation, but also enhance long-range order in the polymer blend. Moreover, the larger CCL achieved in LBL-TL than that of LBL-CF is consistent with the results observed in neat films which supports the improved charge carrier mobility and FF in LBL-TL devices.

Based on our comprehensive study covering FLAS, TEM, RSoXS, and GIWAXS characterizations, a schematic illustration of morphological pictures of BHJ-CB, BHJ-CF, LBL-CF, and LBL-TL films are illustrated in **Figure 4e**. Although the degree of phase separation can be changed to a limited extent in BHJ-CB and BHJ-CF blends, the LBL method can help populate domains with proper sizes and afford a vertically gradient material distribution. By changing the top-layer processing solvent from CF to TL, both the backbone orientation of D18 and the crystallinity of D18 and PY-FT are optimized

to afford a finely tuned blend morphology in D18/PY-FT system for achieving higher photovoltaic performance.

2.5. Evaluation of Device Stability

The stability tracked under continuous illumination at maximum power point (MPP) was investigated based on the optimum BHJ and LBL devices (BHJ-CF and LBL-TL). After MPP tracking for 90 min, the PCE of the BHJ-CF device decays by 5.6%, while the LBL-TL device shows a smaller decay with PCE decreased by only 3.9% (**Figure S23**). The long-term thermal stability of BHJ-CF and LBL-TL devices was also evaluated, while the representative small-molecule Y6-based LBL device with D18 as the donor was used as a reference for comparison. As shown in **Figure 5**, after being heated at 65 °C for 1300 h, the LBL-TL device could retain 92.1% of its initial PCE, whereas the BHJ-CF device showed larger decay to 86.4% in the same duration. A same decaying trend was observed for these two types of devices at a higher aging temperature yet having larger degradation rate (**Figure S24**). The superior stability against thermal stress and continuous illumination of LBL-TL over BHJ-CF indicates the morphological stability of films formed from swelling-induced intermixing may be better than those quenched kinetically. On the contrary, the LBL device based on D18/Y6 suffered a rapid decay to 86% of its initial PCE after only 600 h aging at 65 °C (**Figure S25**). The morphological evolution after thermal annealing for the three films was analyzed by using AFM (**Figure S26**). The surface textures for both the BHJ and LBL all-polymer blends show an indiscernible variation after being annealed at 65°C for ~ 700 h, accounting for the excellent thermal stability. In contrast, a clearly increased aggregation was observed for Y6-based films due to the faster diffusion kinetics under thermal stress, leading to the drastic performance degradation.

This article is protected by copyright. All rights reserved.

3. Conclusions

In this work, we demonstrate a top-down controlling strategy based on LBL deposition to assist the formation of optimum morphology for all-polymer blend. A comprehensive investigation including FLAS, TEM, and RSoXS illustrates such two-step procedure allows the low-miscibility D18/PY-FT system to form a favorably phase-separated morphology by manipulating the swelling of D18 bottom layer to alleviate the formation of oversized domains of aggregated polymers in conventional BHJ films. Instead, a gradient vertical phase distribution is formed to facilitate optimal charge carrier transport and extraction. In addition, the GIWAXS analysis reveals that LBL processing solvents can effectively influence both molecular orientation and packing of D18 bottom layer and the crystallinity of PY-FT layer on top, opening up possibilities to further optimize all-polymer blend morphology. All-PSCs derived from this process afford a high PCE of 17.0% with a remarkable FF of 76.1%, which is much higher than that (15.4%) of the conventional BHJ devices. More importantly, an excellent long-term thermal stability can be realized in the LBL devices, which retains over 90% of its initial PCE after being thermally annealed at 65 °C for 1300 h. Our work provides a facile and effective strategy to control the phase separation and polymer packing simultaneously for achieving high-performance all-PSCs.

Supporting Information

Supporting Information is available from the Wiley Online Library or from the author.

Conflicts of interest

The authors declare no conflict of interest.

This article is protected by copyright. All rights reserved.

Acknowledgements

H.F., Z.P., Q.F., and F.R.L. contributed equally to this work. A.K.Y.J. thanks the sponsorship of the Lee Shau-Kee Chair Professor (Materials Science), and the support from the APRC Grant of the City University of Hong Kong (9380086), the US Office of Naval Research (N00014-20-1-2191), the GRF grant (11307621) and the CRF grant (C6023-19GF) from the Research Grants Council of Hong Kong, Guangdong Major Project of Basic and Applied Basic Research (2019B030302007), Guangdong-Hong Kong-Macao Joint Laboratory of Optoelectronic and Magnetic Functional Materials (2019B121205002). H.Y.W. is thankful for the financial support from the National Research Foundation (NRF) of Korea (2016M1A2A2940911, 2020M3H4A3081814). Z.P. and H.A. gratefully acknowledge the support from the US Office of Naval Research (N000142012155). X-ray data were acquired at beamlines 11.0.1.2, and 7.3.3 at the Advanced Light Source, LBNL, which is supported by the Director, Office of Science, Office of Basic Energy Sciences, of the U.S. Department of Energy under Contract No. DE-AC02-05CH11231.

References

- [1] C. Yan, S. Barlow, Z. Wang, H. Yan, A. K.-Y. Jen, S. R. Marder, X. Zhan, *Nat. Rev. Mater.* **2018**, *3*, 18003.
- [2] G. Wang, F. S. Melkonyan, A. Facchetti, T. J. Marks, *Angew Chem. Int. Ed.* **2019**, *58*, 4129.
- [3] C. Lee, S. Lee, G. U. Kim, W. Lee, B. J. Kim, *Chem. Rev.* **2019**, *119*, 8028.
- [4] Q. Fan, W. Su, S. Chen, W. Kim, X. Chen, B. Lee, T. Liu, U. A. Méndez-Romero, R. Ma, T. Yang, W. Zhuang, Y. Li, Y. Li, T.-S. Kim, L. Hou, C. Yang, H. Yan, D. Yu, E. Wang, *Joule* **2020**, *4*, 658.
- [5] T. Kim, J. H. Kim, T. E. Kang, C. Lee, H. Kang, M. Shin, C. Wang, B. Ma, U. Jeong, T. S. Kim, B. J. Kim, *Nat. Commun.* **2015**, *6*, 8547.

This article is protected by copyright. All rights reserved.

- [6] C. R. McNeill, *Energy Environ. Sci.* **2012**, *5*, 5653.
- [7] J. Du, K. Hu, J. Zhang, L. Meng, J. Yue, I. Angunawela, H. Yan, S. Qin, X. Kong, Z. Zhang, B. Guan, H. Ade, Y. Li, *Nat. Commun.* **2021**, *12*, 5264.
- [8] H. Sun, B. Liu, Y. Ma, J. W. Lee, J. Yang, J. Wang, Y. Li, B. Li, K. Feng, Y. Shi, B. Zhang, D. Han, H. Meng, L. Niu, B. J. Kim, Q. Zheng, X. Guo, *Adv. Mater.* **2021**, *33*, 2102635.
- [9] R. Sun, W. Wang, H. Yu, Z. Chen, X. Xia, H. Shen, J. Guo, M. Shi, Y. Zheng, Y. Wu, W. Yang, T. Wang, Q. Wu, Y. Yang, X. Lu, J. Xia, C. J. Brabec, H. Yan, Y. Li, J. Min, *Joule* **2021**, *5*, 1548.
- [10] J. Zhang, C. H. Tan, K. Zhang, T. Jia, Y. Cui, W. Deng, X. Liao, H. Wu, Q. Xu, F. Huang, Y. Cao, *Adv. Energy Mater.* **2021**, *11*, 2102559.
- [11] Y. Zhang, B. Wu, Y. He, W. Deng, J. Li, J. Li, N. Qiao, Y. Xing, X. Yuan, N. Li, C. J. Brabec, H. Wu, G. Lu, C. Duan, F. Huang, Y. Cao, *Nano Energy* **2022**, *93*, 106858.
- [12] H. Fu, Q. Fan, W. Gao, J. Oh, Y. Li, F. Lin, F. Qi, C. Yang, T. J. Marks, A. K.-Y. Jen, *Sci. China Chem.* **2021**, *65*, 309.
- [13] Q. Fan, H. Fu, Z. Luo, J. Oh, B. Fan, F. Lin, C. Yang, A. K.-Y. Jen, *Nano Energy* **2022**, *92*, 106718.
- [14] H. Fu, Y. Li, J. Yu, Z. Wu, Q. Fan, F. Lin, H. Y. Woo, F. Gao, Z. Zhu, A. K.-Y. Jen, *J. Am. Chem. Soc.* **2021**, *143*, 2665.
- [15] Q. Fan, H. Fu, Q. Wu, Z. Wu, F. Lin, Z. Zhu, J. Min, H. Y. Woo, A. K.-Y. Jen, *Angew. Chem. Int. Ed.* **2021**, *60*, 15935.
- [16] Y. Cui, Y. Xu, H. Yao, P. Bi, L. Hong, J. Zhang, Y. Zu, T. Zhang, J. Qin, J. Ren, Z. Chen, C. He, X. Hao, Z.

This article is protected by copyright. All rights reserved.

Wei, J. Hou, *Adv. Mater.* **2021**, *33*, 2102420.

- [17] C. Li, J. Zhou, J. Song, J. Xu, H. Zhang, X. Zhang, J. Guo, L. Zhu, D. Wei, G. Han, J. Min, Y. Zhang, Z. Xie, Y. Yi, H. Yan, F. Gao, F. Liu, Y. Sun, *Nat. Energy* **2021**, *6*, 605.
- [18] F. Lin, K. Jiang, W. Kaminsky, Z. Zhu, A. K.-Y. Jen, *J. Am. Chem. Soc.* **2020**, *142*, 15246.
- [19] J. Yuan, Y. Zhang, L. Zhou, G. Zhang, H.-L. Yip, T.-K. Lau, X. Lu, C. Zhu, H. Peng, P. A. Johnson, M. Leclerc, Y. Cao, J. Ulanski, Y. Li, Y. Zou, *Joule* **2019**, *3*, 1140.
- [20] G. Yu, G. Gao, J. C. Hummelen, F. Wudl, H. J. Heeger, *Science* **1995**, *270*, 1789.
- [21] G. Li, R. Zhu, Y. Yang, *Nat. Photonics* **2012**, *6*, 153.
- [22] C. J. Brabec, M. Heeney, I. McCulloch, J. Nelson, *Chem. Soc. Rev.* **2011**, *40*, 1185.
- [23] J. Hou, O. Inganäs, R. H. Friend, F. Gao, *Nat. Mater.* **2018**, *17*, 119.
- [24] M. Schubert, B. A. Collins, H. Mangold, I. A. Howard, W. Schindler, K. Vandewal, S. Roland, J. Behrends, F. Kraffert, R. Steyrleuthner, Z. Chen, K. Fostiropoulos, R. Bittl, A. Salleo, A. Facchetti, F. Laquai, H. W. Ade, D. Neher, *Adv. Funct. Mater.* **2014**, *24*, 4068.
- [25] L. Ye, X. Jiao, M. Zhou, S. Zhang, H. Yao, W. Zhao, A. Xia, H. Ade, J. Hou, *Adv. Mater.* **2015**, *27*, 6046.
- [26] K. Zhou, Y. Wu, Y. Liu, X. Zhou, L. Zhang, W. Ma, *ACS Energy Lett.* **2019**, *4*, 1057.
- [27] Y. Wang, X. Zhan, *Adv. Energy Mater.* **2016**, *6*, 1600414.
- [28] K. Jiang, J. Zhang, Z. Peng, F. Lin, S. Wu, Z. Li, Y. Chen, H. Yan, H. Ade, Z. Zhu, A. K.-Y. Jen, *Nat.*

This article is protected by copyright. All rights reserved.

Commun. **2021**, *12*, 468.

- [29] K. Weng, L. Ye, L. Zhu, J. Xu, J. Zhou, X. Feng, G. Lu, S. Tan, F. Liu, Y. Sun, *Nat. Commun.* **2020**, *11*, 2855.
- [30] R. Sun, J. Guo, C. Sun, T. Wang, Z. Luo, Z. Zhang, X. Jiao, W. Tang, C. Yang, Y. Li, J. Min, *Energy Environ. Sci.* **2019**, *12*, 384.
- [31] R. Sun, Q. Wu, J. Guo, T. Wang, Y. Wu, B. Qiu, Z. Luo, W. Yang, Z. Hu, J. Guo, M. Shi, C. Yang, F. Huang, Y. Li, J. Min, *Joule* **2020**, *4*, 407.
- [32] M. Ghasemi, L. Ye, Q. Zhang, L. Yan, J. H. Kim, O. Awartani, W. You, A. Gadisa, H. Ade, *Adv. Mater.* **2017**, *29*, 1604603.
- [33] M. Li, Q. Wang, J. Liu, Y. Geng, L. Ye, *Mater. Chem. Front.* **2021**, *5*, 4851.
- [34] G. Zhang, R. C. Huber, A. S. Ferreira, S. D. Boyd, C. K. Luscombe, S. H. Tolbert, B. J. Schwartz, *J. Phys. Chem. C* **2014**, *118*, 18424.
- [35] H. Fu, W. Gao, Y. Li, F. Lin, X. Wu, J. H. Son, J. Luo, H. Y. Woo, Z. Zhu, A. K.-Y. Jen, *Small Methods* **2020**, *4*, 2000687.
- [36] P. Cheng, R. Wang, J. Zhu, W. Huang, S. Y. Chang, L. Meng, P. Sun, H. W. Cheng, M. Qin, C. Zhu, X. Zhan, Y. Yang, *Adv. Mater.* **2018**, *30*, 1705243.
- [37] D. Li, C. Guo, X. Zhang, B. Du, P. Wang, S. Cheng, J. Cai, H. Wang, D. Liu, H. Yao, J. Hou, T. Wang, *Aggregate* **2021**, DOI: 10.1002/agt2.104.
- [38] Q. Wu, W. Wang, Y. Wu, Z. Chen, J. Guo, R. Sun, J. Guo, Y. Yang, J. Min, *Adv. Funct. Mater.* **2021**,

This article is protected by copyright. All rights reserved.

31, 2010411.

- [39] Y. Xu, J. Yuan, S. Liang, J.-D. Chen, Y. Xia, B. W. Larson, Y. Wang, G. M. Su, Y. Zhang, C. Cui, M. Wang, H. Zhao, W. Ma, *ACS Energy Letters* **2019**, *4*, 2277.
- [40] X. Xu, L. Yu, H. Meng, L. Dai, H. Yan, R. Li, Q. Peng, *Adv. Funct. Mater.* **2021**, *32*, 2108797.
- [41] L. Zhan, S. Li, X. Xia, Y. Li, X. Lu, L. Zuo, M. Shi, H. Chen, *Adv. Mater.* **2021**, *33*, 2007231.
- [42] Y. Cui, H. Yao, J. Zhang, K. Xian, T. Zhang, L. Hong, Y. Wang, Y. Xu, K. Ma, C. An, C. He, Z. Wei, F. Gao, J. Hou, *Adv. Mater.* **2020**, *32*, 1908205.
- [43] J. Lee, D. H. Sin, J. A. Clement, C. Kulshreshtha, H. G. Kim, E. Song, J. Shin, H. Hwang, K. Cho, *Macromolecules* **2016**, *49*, 9358.
- [44] Y. Zhang, K. Liu, J. Huang, X. Xia, J. Cao, G. Zhao, P. W. K. Fong, Y. Zhu, F. Yan, Y. Yang, X. Lu, G. Li, *Nat. Commun.* **2021**, *12*, 4815.
- [45] H. Ning, Q. Jiang, P. Han, M. Lin, G. Zhang, J. Chen, H. Chen, S. Zeng, J. Gao, J. Liu, F. He, Q. Wu, *Energy Environ. Sci.* **2021**, *14*, 5919.
- [46] L. Bu, S. Gao, W. Wang, L. Zhou, S. Feng, X. Chen, D. Yu, S. Li, G. Lu, *Adv. Elect. Mater.* **2016**, *2*, 1600359.
- [47] J. Wang, J. Zhang, Y. Xiao, T. Xiao, R. Zhu, C. Yan, Y. Fu, G. Lu, X. Lu, S. R. Marder, X. Zhan, *J. Am. Chem. Soc.* **2018**, *140*, 9140.
- [48] J. C. Aguirre, S. A. Hawks, A. S. Ferreira, P. Yee, S. Subramaniyan, S. A. Jenekhe, S. H. Tolbert, B. J. Schwartz, *Adv. Energy Mater.* **2015**, *5*, 1402020.

This article is protected by copyright. All rights reserved.

- [49] L. Ye, S. Li, X. Liu, S. Zhang, M. Ghasemi, Y. Xiong, J. Hou, H. Ade, *Joule* **2019**, *3*, 443.
- [50] H. Yin, J. Yan, J. K. W. Ho, D. Liu, P. Bi, C. H. Y. Ho, X. Hao, J. Hou, G. Li, S. K. So, *Nano Energy* **2019**, *64*, 103950.
- [51] H. Chen, T. Zhao, L. Li, P. Tan, H. Lai, Y. Zhu, X. Lai, L. Han, N. Zheng, L. Guo, F. He, *Adv. Mater.* **2021**, *33*, 2102778.
- [52] Y. Firdaus, V. M. Le Corre, S. Karuthedath, W. Liu, A. Markina, W. Huang, S. Chatopadhyay, M. M. Nahid, M. I. Nugraha, Y. Lin, A. Seitkhan, A. Basu, W. Zhang, I. McCulloch, H. Ade, J. Labram, F. Laquai, D. Andrienko, L. J. A. Koster, T. D. Anthopoulos, *Nat. Commun.* **2020**, *11*, 5220.
- [53] L. Ye, Y. Xiong, S. Li, M. Ghasemi, N. Balar, J. Turner, A. Gadisa, J. Hou, B. T. O'Connor, H. Ade, *Adv. Funct. Mater.* **2017**, *27*, 1702016.
- [54] J. S. Park, N. Choi, C. Lee, S. Lee, J.-W. Ha, D.-H. Hwang, B. J. Kim, *Chem. Mater.* **2020**, *32*, 3585.

Table 1. Summary of photovoltaic performance parameters of all-PSCs based on D18 and PY-FT processed with different conditions.

Devices	V_{oc} (V)	J_{sc} (mA/cm ²)	J_{cal}^a (mA/cm ²)	FF (%)	PCE ^b (%)
---------	-----------------	-----------------------------------	--------------------------------------	-----------	-------------------------

This article is protected by copyright. All rights reserved.

BHJ-CB	0.940	21.6	20.9	68.5	13.9 (13.7±0.2)
BHJ-CF	0.923	23.1	22.3	72.3	15.4 (15.1±0.3)
LBL-CF	0.919	23.6	22.9	74.5	16.2 (15.9±0.3)
LBL-TL	0.925	24.2	23.6	76.1	17.0 (16.8±0.2)

^aIntegrated from EQE spectra. ^bThe average parameters were calculated from over 10 devices.

Table 2. RSoXS Characteristics of BHJ-CB, BHJ-CF, LBL-CF, and LBL-TL blends.

Blends	Peak1 q_1 (nm ⁻¹)	Long period (nm)	Average domain size (nm)	Volume fraction (%)	Peak2 q_2 (nm ⁻¹)	Long period (nm)	Average domain size (nm)	Volume fraction (%)	Relative integrated scattering intensity (ISI)
BHJ-CB	0.066	95	47.5	59	0.234	27	13.5	41	1
BHJ-CF	0.07	90	45	42	0.221	28	14	58	0.98
LBL-CF	0.037	169	84.5	38	0.22	29	14.5	62	0.93
LBL-TL	0.0478	131	65.5	13	0.24	26	13	87	0.92

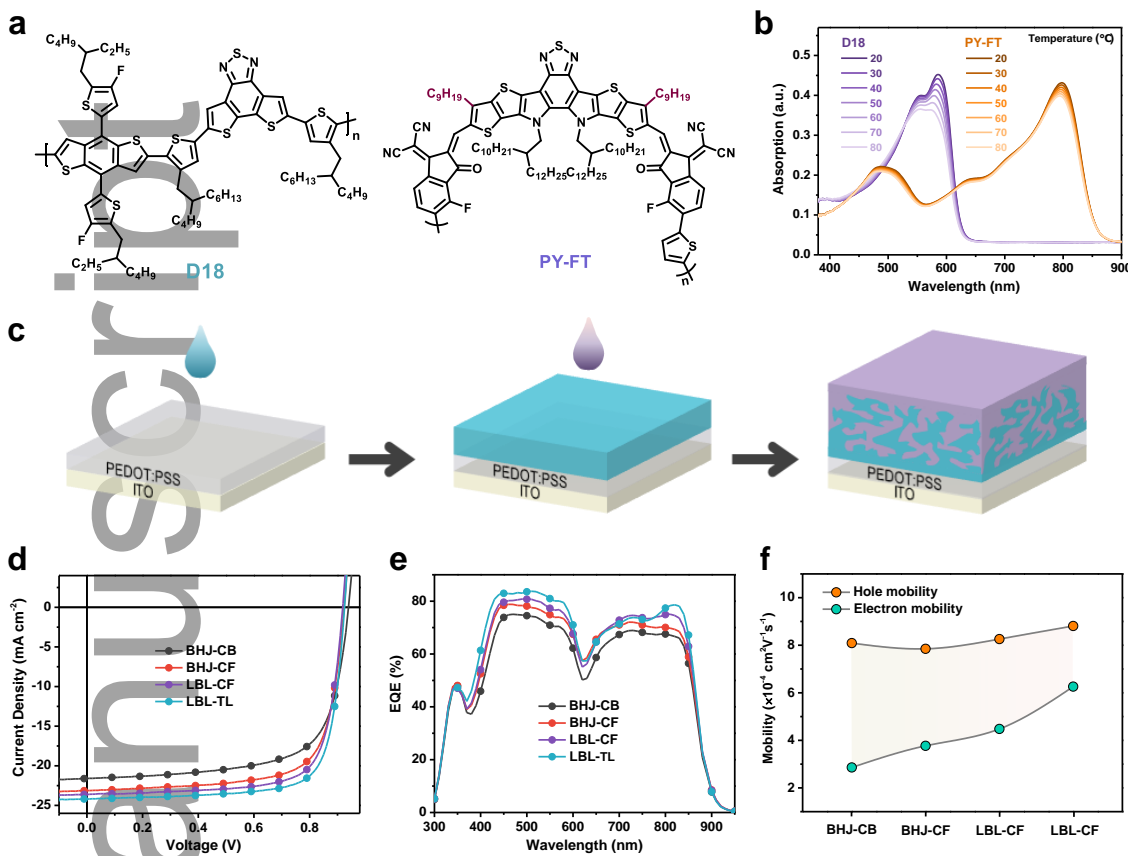


Figure 1. (a) Chemical structures of D18 and PY-FT. (b) Variable temperature UV-vis absorption spectra of D18 and PY-FT in dilute CB solutions. (c) Schematic diagram of the layer-by-layer depositing procedure. (d) *J-V* curves and (e) the corresponding EQE spectra for the four types of all-PSCs based on D18 and PY-FT prepared with different conditions. (f) SCLC electron and hole mobilities for BHJ-CB, BHJ-CF, LBL-CF, and LBL-TL blends.

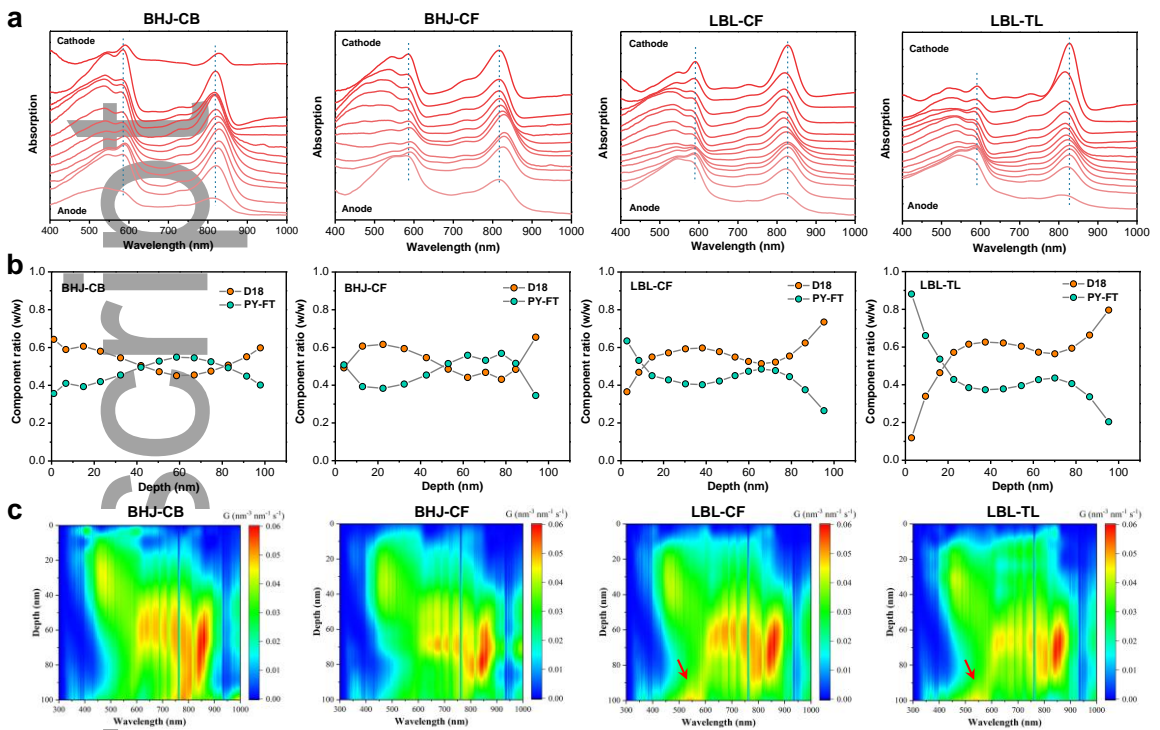


Figure 2. (a) Film-depth-dependent light absorption spectra (the sub-layer thickness for each spectrum is approximately 10 ± 2 nm), (b) composition distribution and (c) exciton generation contour as a function of film depth for BHJ-CB, BHJ-CF, LBL-CF, and LBL-TL blend films, where depth 0 and 100 nm represent the PNDIT-F3N/active layer and PEDOT:PSS/active layer interfaces, respectively. For exciton generation contour, the incident light is from the ITO/PEDOT:PSS side.

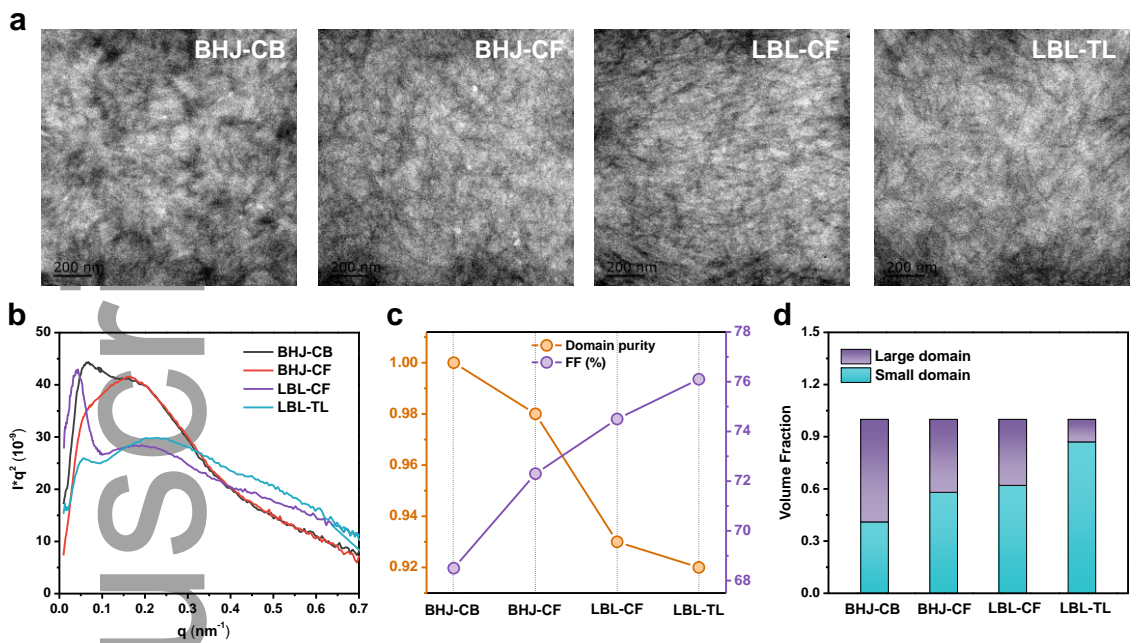


Figure 3. (a) TEM images and (b) Lorentz corrected RSoXS profiles acquired at 284 eV for BHJ-CB, BHJ-CF, LBL-CF, and LBL-TL films. (c) Correlation analysis of Domain purity-FF relationships for BHJ-CB, BHJ-CF, LBL-CF, and LBL-TL devices. (d) Domain distributions in the BHJ-CB, BHJ-CF, LBL-CF, and LBL-TL films. The large domain is much larger than the typical exciton diffusion length while the small domain is close to exciton diffusion length.

This article is protected by copyright. All rights reserved.

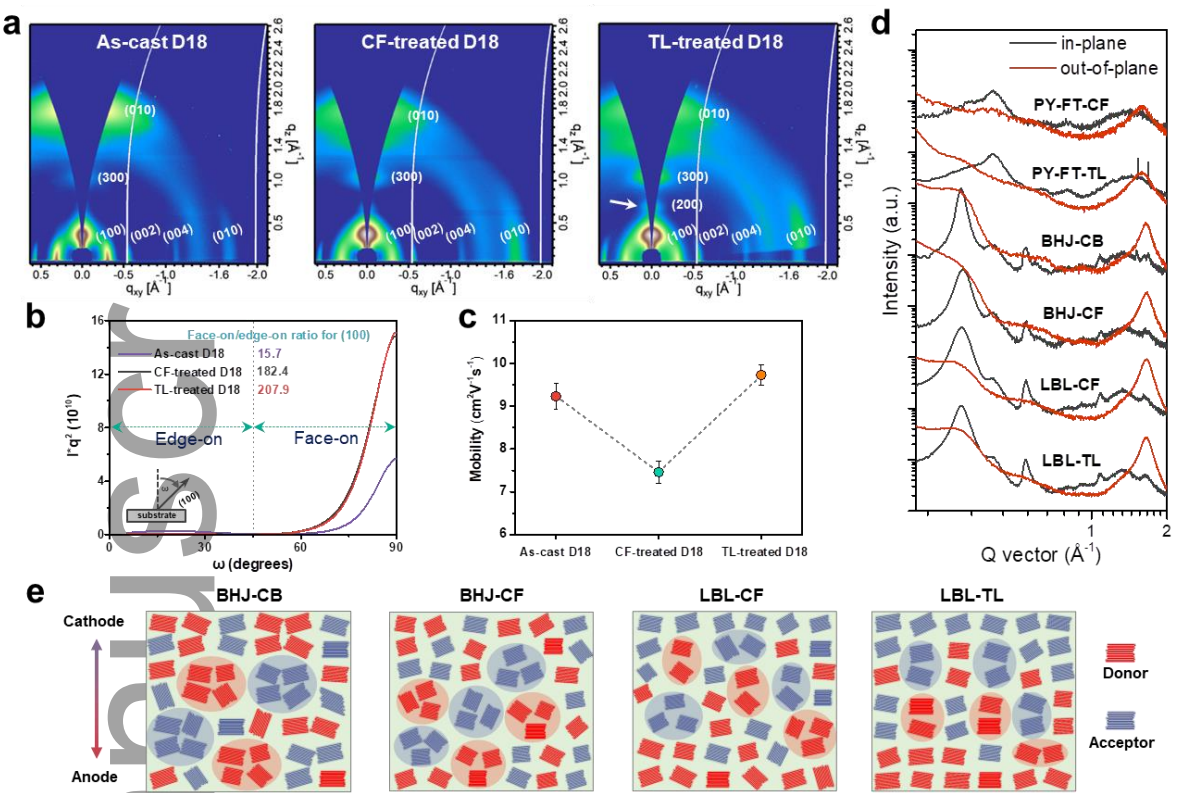


Figure 4. (a) 2D GIWAXS diffraction patterns and (b) the pole figure extracted from (100) scattering peak for the as-cast D18 film as well as D18 films post-treated with neat solvents of CF or TL. The azimuthal angle was defined to be ω , which is the angle with respect to the q_z axis. (c) Hole mobility of as-cast D18 film and CF-, TL-treated D18 films. (d) In-plane and out-of-plane line-cut profiles for CF- and TL-processed neat PY-FT films, and four blend films prepared with different conditions. (e) Schematic illustration of morphology for BHJ-CB, BHJ-CF, LBL-CF, and LBL-TL blends (the colored circles, as a guideline to eyes, represent the D18 or PY-FT phase).

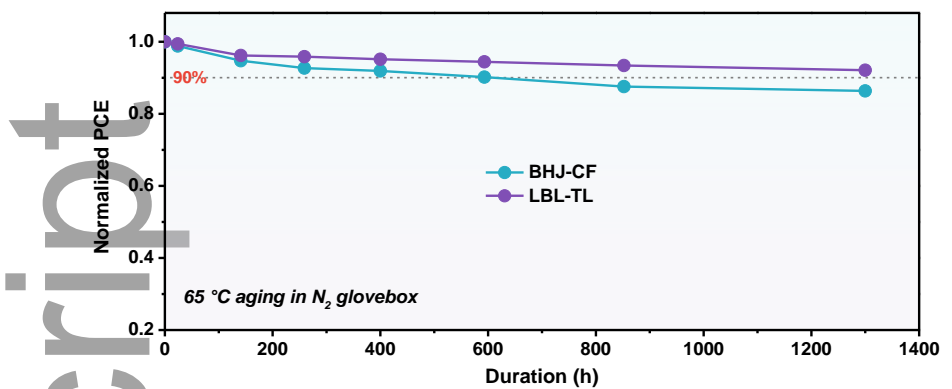


Figure 5. Consecutive thermal stability of optimum BHJ and LBL devices based on D18 and PY-FT. Both devices were non-encapsulated and heated in an N₂-filled glove box at 65 °C.

A facile top-down strategy to control the all-polymer solar cell (all-PSC) morphology is developed by layer-by-layer processing. Optimal intermixing of polymer components could be achieved by tuning the bottom-layer polymer swelling during top-layer deposition. Both molecular orientation/packing of bottom layer and crystallinity of top layer can be optimized with a suitable top-layer processing solvent. Consequently, a favorable morphology with gradient vertical composition distribution is realized, affording a high all-PSC efficiency of 17.0%.

Huiting Fu, Zhengxing Peng, Qunping Fan, Francis R. Lin, Feng Qi, Yixin Ran, Ziang Wu, Baobing Fan, Kui Jiang, Han Young Woo, Guanghao Lu, Harald Ade,* and Alex K.-Y. Jen*

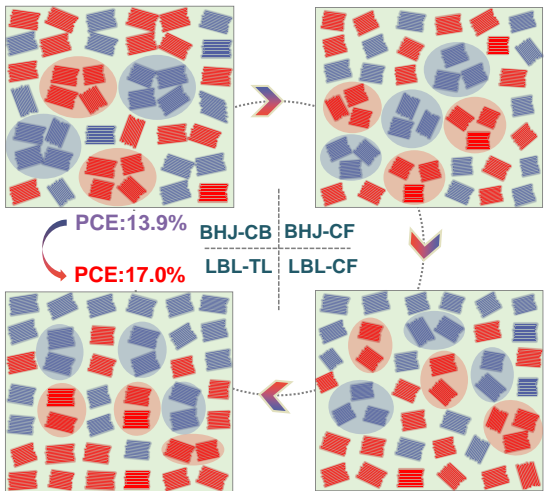
A Top-down Strategy to Engineer Active Layer Morphology for Highly Efficient and Stable All-polymer Solar Cells

ToC Figure

This article is protected by copyright. All rights reserved.

Author Manuscript

WILEY-VCH



This article is protected by copyright. All rights reserved.